J Mater Sci: Mater Electron (2023) 34:1528

Effect of Mn substitution-driven structural transition on magnetic and optical properties of multiferroic $Bi_{0.85}La_{0.15}FeO_3$ ceramics

Mukesh Shekhar[1], Sonu Rani[2], Rabichandra Pandey[3], Lawrence Kumar[4], Manoranjan Kar[3], and Pawan Kumar[1,*]

[1] Department of Physics, Mahatma Gandhi Central University, Bihar 845401, India
[2] Department of Physics, Magadh Mahila College, Patna University, Patna 800001, India
[3] Department of Physics, Indian Institute of Technology Patna, Bihta, Patna 801103, India
[4] Department of Metallurgical & Materials Engineering, Central University of Jharkhand, Ranchi 835205, India

Received: 25 April 2023
Accepted: 7 July 2023
Published online: 15 July 2023

ABSTRACT

$Bi_{0.85}La_{0.15}FeO_3$, a Lanthanum (La) modified form of bismuth ferrite (BFO) crystallizes to crystal structure which is free from any impurity, which improves the multiferroic properties of BFO. To achieve the enhanced multiferroic characteristics, the composition of $Bi_{0.85}La_{0.15}FeO_3$ has been optimized with the Mn substitution which increases magnetization more effectively than those of magnetic cations. Therefore, $Bi_{0.85}La_{0.15}Fe_{1-x}Mn_xO_3$ polycrystalline samples were synthesized using a tartaric acid modified sol–gel technique for x = 0.000, 0.025, 0.050, and 0.100. The effects of substitution of Mn (non-magnetic in nature) at the Fe site on crystal structure, magnetic properties, and optical properties were then investigated. The formation of crystalline phases was checked by using X-ray diffraction. The structural transition from rhombohedral (*R3c*, space group) to orthorhombic (*Pbnm*, space group) is strongly supported by the Rietveld refinement of the XRD pattern as well as analysis of Raman spectra. As Mn substitution increases, the intensity of Raman peak at about 650 cm^{-1} increases as well, indicating an increase in the contribution of orthorhombic phase. Magnetic properties of $Bi_{0.85}La_{0.15}Fe_{1-x}Mn_xO_3$ polycrystalline samples were assessed at room temperature. In $Bi_{0.85}La_{0.15}Fe_{1-x}Mn_xO_3$, the Mn substitution at the Fe site produced the highest magnetic moment for x = 0.025. Magnetic hysteresis loops show a substantial change in the magnetization with the increase in Mn substitution. Using the Kubelka–Munk (K–M) function and Tauc plot, the band gap energies of all the samples were calculated from UV–Vis diffuse reflectance spectra and it was observed that the band gap energy decreases with the increase in Mn substitution in $Bi_{0.85}La_{0.15}Fe_{1-x}Mn_xO_3$. These findings provide better understanding for tuning of the multiferroic properties of Mn substituted $Bi_{0.85}La_{0.15}FeO_3$ ceramics.

Address correspondence to E-mail: pawankumarmgcub@gmail.com

https://doi.org/10.1007/s10854-023-10962-1

1 Introduction

Multiferroic materials exhibit unique characteristic due to the simultaneous existence of two or more ferroic orders in the same phase. Because of the interlinkage between ferroelectric and magnetic domain in multiferroic material, it becomes easy to tune the properties of material. Hence, we can say that these materials are very rare and attracted a lot of attention worldwide [1–3]. These materials are used in a broad variety of electronic devices, including sensors, spintronic devices, data storage devices, memory devices etc. [2, 4]. Amongst all the known multiferroic BFO (bismuth ferrite) is the most attracting materials because of the existence of multiferroic properties at room. It is having ferroelectric ordering or polarization with high Curie temperature T_C = 1103 K and an anti-ferromagnetic ordering with Neel temperature T_N = 647 K [5]. In BFO, structural distortions caused by the stereochemical activity of the $6s^2$ lone pair electrons of Bi^{3+} create ferroelectricity. At room temperature BFO exhibits anti-ferromagnetism along with G-type spiral spin configuration having periodicity of 620 Å. This ordering superimposed with cycloidal spin structure cancels the macroscopic magnetizations and give rise to magnetoelectric effect [6]. Despite the peculiar properties of bulk BFO, there are several problems associated with it, like high leakage current, poor ferroelectric behavior, appearance of impurity phases, very low value of saturation magnetization etc. Hence, the performance of bulk BFO in real technological applications is not up to the mark as compared with other multiferroic material such as CuO, $Pb(Fe,Ta,Zr,Ti)O_3$, $Pb(Fe,W,Zr,Ti)O_3$, $Sr_3Co_2F_{24}O_{41}$ etc. [7]. One of the drawbacks associated with BFO is poor ferroelectric behavior which arises due to existence of impurity phases. The amount of impurity phases can also be controlled by variation in annealing temperature and hence helps in changing the multiferroic properties of material [8]. Several other strategies have been proposed in order to improve the properties of BFO. One of the best strategies is to improve multiferroic properties by doping/substitution. The doping induces a convergence between the ferroelectric transition temperature and ferromagnetic transition temperature, which leads to increased magnetoelectric coupling and hence improves the properties of multiferroic material.

Many researchers have carried out Bi site substitution with alkaline earth metal ions or rare earth ions (Nd, Gd, Pr, Dy, Cr etc.) and Fe site substitution with transition metal ions (Ti, Zr, Nb, Mn etc.) to improve the multiferroic properties of BFO. Some researchers reported that after substitution of Ca at B-site of pure BFO, the net magnetization increases because of suppressed spin spiral structure [9]. Co-doping at the A-site and B-site of BFO is a successful approach to improve the multiferroic properties of bismuth ferrite by decreasing band gap and the variation in Fe–O–Fe bond angle [10]. La and Mn co-doped BFO shows structural transition along with the improved magnetization of BFO [11]. Doping also improves the multiferroic properties of material by cation size effect of dopants [12–14]. Also the substitution of La and Mn in BFO shows the decrease in band gap, particle sizes [15–17]. Co-doping in BFO by Pr and Zr [18], Pr and Ti [19], Dy and Mn [20], Ca and Mn [21] etc. shows enhanced multiferroic properties. According to reports, the Mn substitution at the Fe site of bismuth ferrite prevented growth of grain, which reduced the size of the particles [22] and results improvement of electrical as well as magnetic properties [23, 24]. The structural phase transition in Mn doped BFO ceramics, which led to a significant increase in magnetism, was also reported by other researchers [25]. The resistivity, dielectric constant, and multiferroic characteristics of lanthanum modified BFO are improved by stabilizing the nonuniformity in the spiral spin structure [26, 27]. According to reports, $Bi_{0.85}La_{0.15}FeO_3$ is a impurity phase-free BFO with increased magnetization due to distortion in spiral spin structure [28]. Mn and transition metal co-doped BFO gives rise to the modification in the band gap [29]. According to Cheng et al. [6] $Bi_{1-x}La_xFeO_3$ ceramics with x = 0, 0.1, 0.2, and 0.3 were prepared by solid-state reaction and it preserves the rhombohedral shape of BFO below 10% La doping. However, for $Bi_{0.7}La_{0.3}FeO_3$ and $Bi_{0.8}La_{0.2}FeO_3$ the structure becomes tetragonal and orthorhombic, respectively. According to the authors, doping of Mn improves the photovoltaic effect and significantly reduces electric leakage [30].

Therefore, it is reasonable to assume that Mn substituted $Bi_{0.85}La_{0.15}FeO_3$ at its Fe-site will exhibit improved multiferroic properties. To the best of our knowledge, no thorough research on the effects of crystal structure change on physical properties has been done on Mn substituted $Bi_{0.85}La_{0.15}FeO_3$

($Bi_{0.85}La_{0.15}Fe_{1-x}Mn_xO_3$). This triggers our interest in creating Mn substituted $Bi_{0.85}La_{0.15}FeO_3$ nanocrystallites using a modified tartaric acid sol–gel technique and examining the impact of substitution on the sample's structure, surface morphology, magnetic properties, and optical properties.

2 Experimental

2.1 Synthesis of material

The polycrystalline samples of $Bi_{0.85}La_{0.15}Fe_{1-x}Mn_xO_3$ with x = 0.000, 0.025, 0.050, and 0.100 were synthesized by the tartaric acid modified sol–gel technique [31]. The bismuth nitrate pentahydrate (≥ 98% pure, Alfa Aesar), iron nitrate nonahydrate (≥ 98% pure, Alfa Aesar), lanthanum acetate (≥ 99.9% pure, Alfa Aesar), manganese acetate (≥ 99% pure, Alfa Aesar) and tartaric acid (≥ 99% pure, Merck) were used as starting materials and were carefully weighted in stoichiometric proportion. The molar ratio of tartaric acid to all metal nitrates was 1:2. The metal nitrates were dissolved in concentration nitric acid in different beakers, while the acetate and tartaric acid were dissolved in deionized water (milli Q grade). Method of sonication was used to create corresponding solutions. The ultimate solution was created in a single beaker by combining all of the previous solutions. Using a hot plate and magnetic stirrer, the mixed solution was heated to 80 °C while being stirred continuously. The liquid eventually became more viscous and turned into gel form. To remove any excess water, the gel was dried in an oven set at 100 °C for the entire night. After drying, the gel became a fluffy mass, which eventually shattered into brittle flakes. The resultant flake was grounded and the final obtained mixture was annealed in a programmed furnace (having 5 °C/min ramp rate) for three hours, using alumina crucible at 700 °C.

2.2 Characterization

Using a Rigaku (Japan) Ill diffractometer with CuKα radiation (λ = 1.5418 Å), in a 2θ range of 20–100° at a scan step of 0.02°, the powder X-ray diffraction (XRD) study of all the samples was carried out. Raman spectra were recorded using a room-temperature STR 750 RAMAN Spectrograph and a micro-Raman spectrometer from Seki Technotron Corp. of Japan with 514.5 nm laser line as the source of excitation. The dispersed light was focused and gathered using a 100× microscope. At room temperature, the magnetic hysteresis loop was measured using a superconducting quantum interference device (SQUID) magnetometer from Quantum Design, INC. (USA) with a maximal applied magnetic field of ± 7 T. The band gaps of all the samples were measured using a LAMBDA 35 UV–visible spectrophotometer (diffuse reflectance spectroscopy mode) in the range of 200–900 nm.

3 Results and discussion

3.1 Structural analysis of crystal

Figure 1 shows the room temperature XRD pattern of polycrystalline sample of $Bi_{0.85}La_{0.15}Fe_{1-x}Mn_xO_3$ with x = 0.000, 0.025, 0.050 and 0.100 annealed at 700 °C for 2θ ranging from 20 to 70°.

Figure 2 shows that the crystal structure of BFO at room temperature is characterized by the appearance of characteristic doublet of (104) and (110) peaks around 32° and 32.2°. On increasing the La and Mn content, the above doublet overlap to give a single peak and the systematic shift in the peak position was observed. It is due to the increased lattice strain because of the replacement of Fe by the Mn with smaller ionic radius. In addition, there was no segregation of secondary phases as observed from the

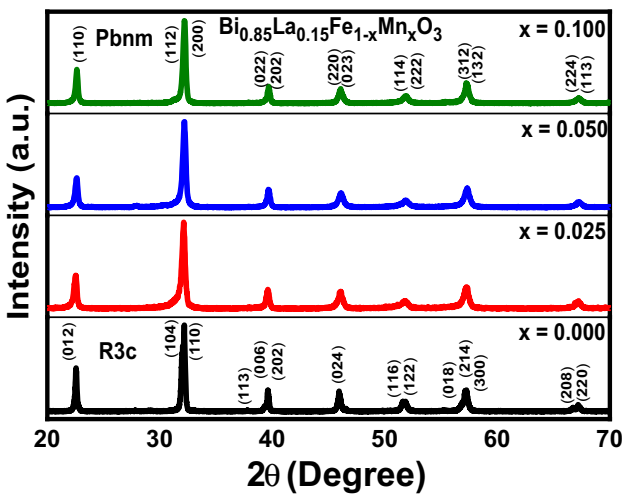

Fig. 1 XRD patterns of $Bi_{0.85}La_{0.15}Fe_{1-x}Mn_xO_3$ for x = 0.000–0.100

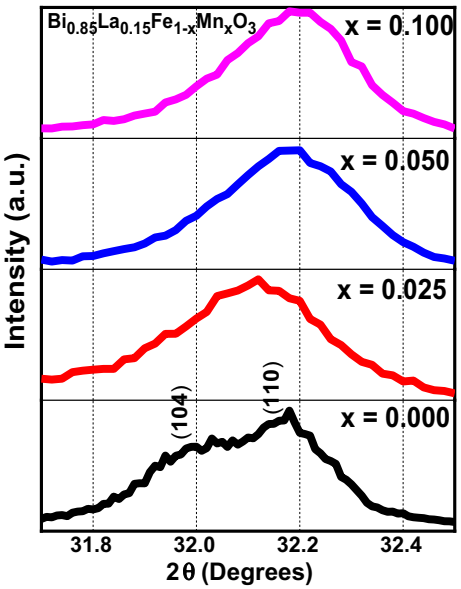

Fig. 2 Shift in the highest intensity peak of XRD patterns of $Bi_{0.85}La_{0.15}Fe_{1-x}Mn_xO_3$ for x = 0.000–0.100

XRD pattern. It can be seen from Fig. 1 that all the peaks which are in the XRD pattern for x = 0.000 are indexed to *R3c* space group and is free from secondary phase. From Fig. 1, it can also be seen that a new indexing with indices (110), (112), (200), (022), (202), (220), (023), (114), (222), (312), (132), (224) and (113) shows the existence of orthorhombic crystal symmetry. Similar kind of phase transition are observed by other researchers also [6, 32, 33]. Using the Williamson Hall plot method, the average crystallite size and lattice strain for all the samples were determined [34].

$$\beta \cos\theta = 4\varepsilon \sin\theta + \frac{k\lambda}{D} \quad (1)$$

In Eq. 1, β (FWHM) is the full width at half maxima of the intensity (a.u.) vs 2 θ profile, λ is the wavelength of the CuKα radiation (λ = 1.5418 Å), D is the average crystallite size, and θ is the Bragg diffraction angle k is shape factor (= 0.89), and ε is the intrinsic strain. The full width at half maxima was corrected by considering instrumental broadening that is given by following equation [35]:

$$\beta = \sqrt{\beta^2_{\text{observed}} - \beta^2_{\text{instrumental}}} \quad (2)$$

Here, $\beta^2_{\text{observed}}$ is the FWHM of the XRD pattern as obtained and $\beta^2_{\text{instrumental}}$ corresponds to the FWHM of the XRD pattern recorded for the pure sample with large crystallites. Table 1 lists the average crystallite size and strain for each sample. It was found that the average crystallite sizes are in the nm range, which is less than the cycloid spin structure (62 nm). Because the ionic size disparity between the Fe and Mn ions prevents crystal formation, the typical crystallite sizes are decreasing as Mn substitution increases. Other researchers have noted comparable outcomes [32, 33, 36, 37]. The Mn substitution causes lattice strain in the material by increasing local structural disorder. As a result, the sample's lattice strain increased along with the amount of Mn substitution. Additionally, it shows how the crystal expanded as Mn substitution increased. Using Fullprof software, the Rietveld refinement of XRD patterns of all the samples was carried out to find out various structural parameters like lattice constants, volume of unit cell, crystallographic phase percentage etc. The expression of FWHM used in Rietveld refinement is given by [38]:

$$\text{FWHM}^2 = \left(U + D^2_{ST}\right)(\tan^2\theta) + V(\tan\theta) + W + \frac{IG}{\cos^2\theta} \quad (3)$$

where, U, V, and W are the usual peak shape parameters, and IG and D_{ST} represents the isotropic size effect and strain-related coefficient respectively. Figure 3 shows the Rietveld refinement of XRD patterns for all the samples using both *R3c* and *Pbnm* space groups.

The lattice parameters and unit cell volume of all the samples obtained after Rietveld refinement using *R3c* and *Pbnm* space groups are also represented in Table1.

Table 1 show that when Mn substitution increases, there is a corresponding fluctuation in the lattice parameters and unit cell volumes of the samples. It confirms that the earlier-discussed structural changes were caused by the XRD peaks shift towards higher angles. Other researchers have also noted comparable outcomes [37, 39, 40]. Table 2 represents the *R3c* and *Pbnm* space groups crystallographic phase percentage of $Bi_{0.85}La_{0.15}Fe_{1-x}Mn_xO_3$ for x = 0.000–0.100, along with the bond angle and goodness of fit parameters (R_F, R_B, R_p, R_{wp}, R_{exp}, and χ^2).

Table 2 demonstrates that with an increase in Mn substitution at the Fe site of $Bi_{0.85}La_{0.15}Fe_{1-x}Mn_xO_3$, the phase contribution from the *R3c*, space group drops while the phase contribution from the *Pbnm*, space group increases. In practice the

Table 1 Structural parameters of $Bi_{0.85}La_{0.15}Fe_{1-x}Mn_xO_3$ ceramics for x = 0.000–0.100

Sample	Average Crystalli-te Size (nm)	Lattice strain	Unit cell volume ($Å^3$)		Lattice parameters (space group, *R3c)*		Lattice parameters (space group, *Pbnm)*		
x			*R3c*	*Pbnm*	a = b (Å)	c (Å)	a (Å)	b (Å)	c (Å)
0.000	36.2	0.00316	369.43	257.90	5.5601	13.7987	5.5956	5.6259	8.1923
0.025	26.7	0.00362	366.37	286.76	5.5557	13.7057	5.6622	6.3888	7.9271
0.050	22.5	0.00384	368.37	278.16	5.5654	13.7338	4.9870	7.1229	7.8304
0.100	18.1	0.00479	369.41	270.34	5.5712	13.7429	5.7660	5.9065	7.9378

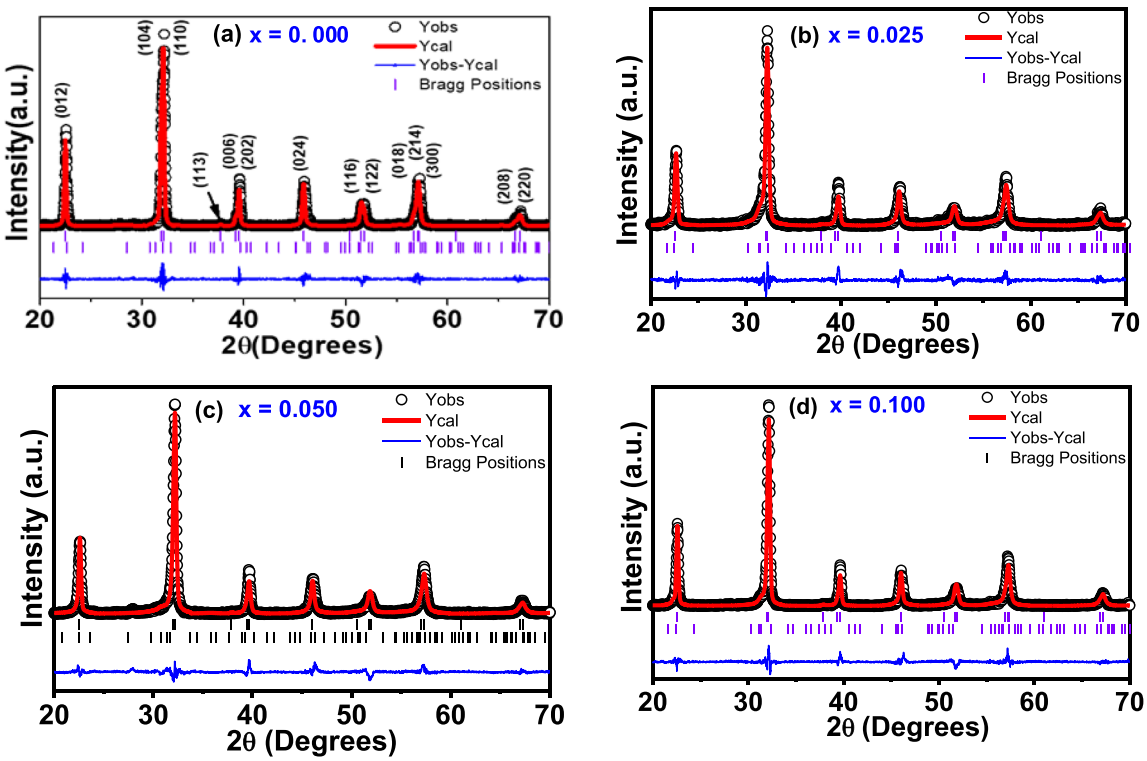

Fig. 3 Rietveld refined XRD patterns of $Bi_{0.85}La_{0.15}Fe_{1-x}Mn_xO_3$ for x = 0.000–0.100

Table 2 Various R–factors (R_F, R_B, R_p, R_{wp}, $R_{exp,}$), goodness of fit (χ^2) and crystallographic phase percentage of $Bi_{0.85}La_{0.15}Fe_{1-x}Mn_xO_3$ ceramics for x = 0.000–0.100

Sample	Crystallographic phase percentage (%)		R-factors					Goodness of fit	Fe–O–Fe bond angle (degree)
x	*R3c*	*Pbnm*	R_F (%)	R_B (%)	R_p (%)	R_{wp} (%)	R_{exp} (%)	χ^2	
0.000	98.82	1.18	5.47	9.04	15.4	23.7	11.19	4.49	176.01
0.025	81.12	18.88	3.99	5.98	18.9	25.9	16.12	2.54	167.73
0.050	37.83	62.17	4.41	6.36	13.1	18.7	10.17	3.38	156.62
0.100	27.66	72.34	4.58	4.93	14.8	21.7	14.86	2.82	156.62

acceptable range of R-factors is < 15, but in our case some of the R-factors are greater than 15, one of the possible reason could be due to the nanocrystallite nature of the sample. The Fe–O–Fe bond angles measured with VESTA software are also included in Table 2. The Fe–O–Fe bond angle decreases when the Mn substitution at the Fe site of $Bi_{0.85}La_{0.15}Fe_{1-x}Mn_xO_3$ increases. Other researchers also observed the substantial change in Fe–O–Fe bond angle due to co-doping [10]. Figure 4a, b represents the crystal structure of *R3c* and *Pbnm* space groups of $Bi_{0.85}La_{0.15}Fe_{1-x}Mn_xO_3$ respectively.

3.2 RAMAN

The use of Raman spectroscopy, a sensitive method based on atomic displacement, on all samples allows researchers to examine how the concentration of substitution affects the samples' structural evolution. According to group theory, *R3c* space group contains 18 optical phonon modes: $4A_1 + 5A_2 + 9E$. Here, A_1 represents the Raman active modes, E modes are IR-active modes and A_2 are silent modes [42]. However, for *Pbnm* space groups with orthorhombic structure, 24 Raman active modes were predicted, including $7A_g + 5B_{1g} + 7B_{2g} + 5B_{3g}$ [43]. Up to 167 cm^{-1} (low number modes), only Bi atom participate and in between 152 and 262 cm^{-1}, Fe atoms contributes in mode formation, and for above 262 cm^{-1} oxygen motion predominates in mode formation, according to Porporati et al. [42]. Figure 5 shows the combined Raman plot of $Bi_{0.85}La_{0.15}Fe_{1-x}Mn_xO_3$ for x = 0.000–0.100. The obtained Raman spectra were deconvoluted into corresponding Lorentzian component and natural frequency of each Raman active mode for all the samples of $Bi_{0.85}La_{0.15}Fe_{1-x}Mn_xO_3$ has been obtained. The Raman spectra along with the deconvoluted curves of $Bi_{0.85}La_{0.15}Fe_{1-x}Mn_xO_3$ for x = 0.000–0.100, has been shown in Fig. 6.

Figure 6 shows that with the increase in Mn substitution the number of Raman active modes gets reduced. The reason could be the presence of large number of point defects and development of local stress [44]. These two phenomenon's collectively causes lowering of symmetry which results in band broadening in Raman spectra. The peak positions of Raman active modes of $Bi_{0.85}La_{0.15}Fe_{1-x}Mn_xO_3$ for x = 0.000–0.100 are represented in Table 3.

The three sharp peaks of $Bi_{0.85}La_{0.15}Fe_{1-x}Mn_xO_3$ for x = 0.000, assigned as A_1-1, A_1-2 and A_1-3, phonon modes are present at around 151, 178 and 238 cm^{-1}. The E modes are assigned to other phonon modes which are located approximately in the range of 270–635 cm^{-1}. With the increase in substitution concentration of Mn, the average mass of A site decreases, because atomic mass of La is about 33% less than the atomic mass of Bi. Since the frequency of Raman

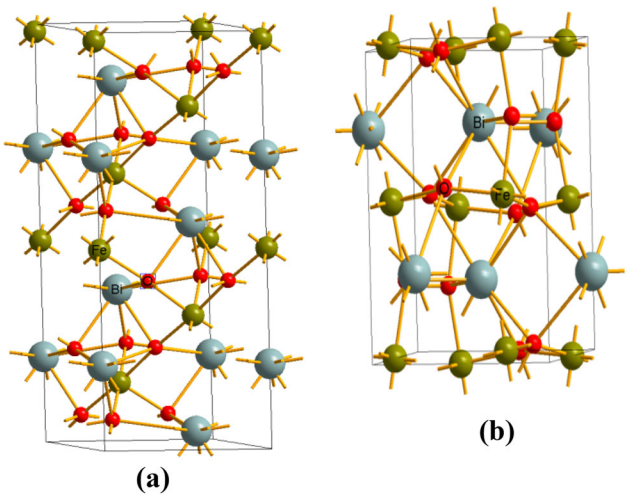

Fig. 4 **a** Rhombohedral (*R3c*, space group) and **b** Orthorhombic, (*Pbnm*, space group) structure of $Bi_{0.85}La_{0.15}Fe_{1-x}Mn_xO_3$ using VESTA software

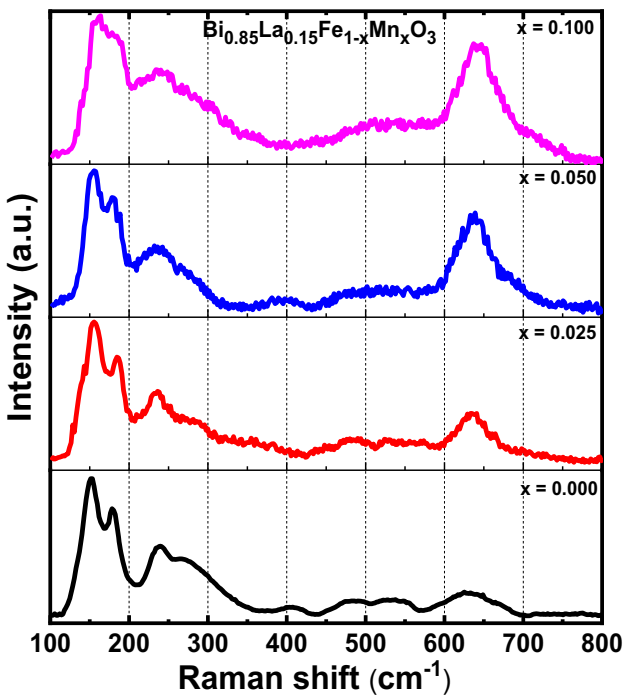

Fig. 5 Combined Raman plot of $Bi_{0.85}La_{0.15}Fe_{1-x}Mn_xO_3$ for x = 0.000–0.100

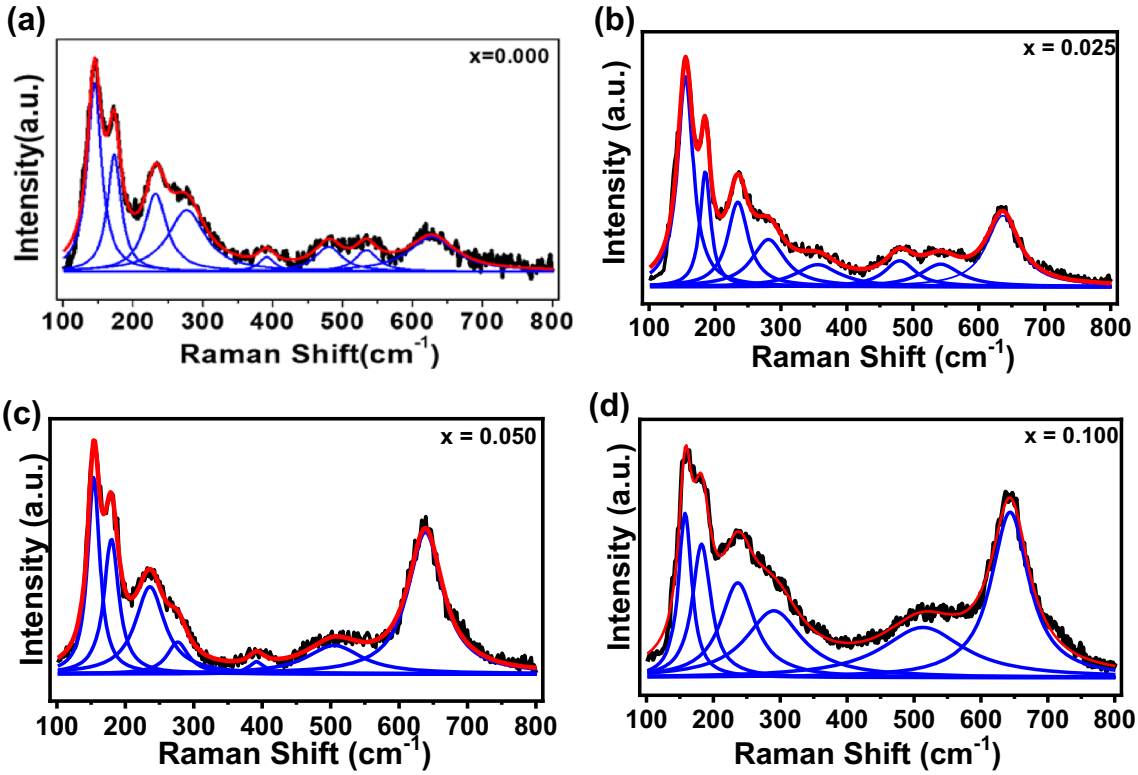

Fig. 6 Deconvolution of Raman plots of $Bi_{0.85}La_{0.15}Fe_{1-x}Mn_xO_3$ for x = 0.000–0.100

Table 3 Observed values of different modes of $Bi_{0.85}La_{0.15}Fe_{1-x}Mn_xO_3$ for x = 0.000–0.100

Raman mode	Observed values of Raman shift (cm^{-1})			
	x = 0.000	x = 0.025	x = 0.050	x = 0.100
A_1-1	151.40	155.56	149.32	157.63
A_1-2	178.37	184.58	180.44	182.51
A_1-3	238.25	234.13	238.25	236.19
E	271.12	281.37	277.27	289.56
E	403.47	356.86	391.33	–
E	485.98	479.96	503.99	513.99
E	537.93	541.91	–	–
E	633.05	636.99	638.96	644.87

mode is proportional to $(K/M)^{1/2}$ where K and M are the reduced mass and force constant respectively. Therefore, with the increase in concentration of Mn substitution the frequency of the phonon modes shifts towards higher frequency side because of the inverse proportionality with reduced mass. From Table 3, it can be seen that A_1-1 and A_1-2 Raman modes shift towards higher frequency side and with the increase in substitution concentration, the intensity of peak A_1-2 increases. Ultimately for x = 0·100, both the peaks merge to form a single peak. Some of the E peaks ranging between 271 and 542 cm^{-1} disappears. The intensity of E peak corresponding to around 640 cm^{-1} increases with the increase in concentration of substitution. These two simultaneous phenomenon first is the disappearance of some Raman modes peaks and second is increase in intensity of the other modes indicates the transition of crystal structure. Similar results of Phase transition from rhombohedral to orthorhombic symmetry was observed by other researchers Wu et al. [45] in bismuth ferrite system under high pressure. Thus, the study of Raman spectra reveals compositional driven phase transition from rhombohedral to orthorhombic with the increase in substitution concentration of Mn at Fe site of $Bi_{0.85}La_{0.15}Fe_{1-x}Mn_xO_3$. Similar kind of results of Raman studies are observed by other researchers also [40, 46].

3.3 Magnetic analysis

The magnetic measurement of $Bi_{0.85}La_{0.15}Fe_{1-x}Mn_xO_3$ for x = 0.000–0.100, has been obtained with an applied field of ±7T using SQUID magnetometer at

room temperature. Figure 7 shows the magnetization (M) vs. magnetic field (H) hysteresis loop for all the samples.

Figure 7 show that each sample exhibits an unsaturated loop and a weak residual magnetism. The canting of the antiferromagnetically ordered spins results from the structural distortion caused by the La replacement, which also increases magnetism. Table 4 represents different magnetic parameters extracted from the M-H loop of $Bi_{0.85}La_{0.15}Fe_{1-x}Mn_xO_3$ for x = 0.000–0.100. For the sample $Bi_{0.85}La_{0.15}Fe_{1-x}Mn_xO_3$ with x = 0.000, the saturation magnetization and remnant magnetization were found to be 0.254 and 0.060 emu/gm respectively. Figure 7 also shows that the Mn substituted sample with x = 0.025, has hysteresis loop with large area and has better magnetic characteristic.

The Mn Substitution at Fe site decreases the Fe–O–Fe bond angle as mentioned in Table 2. This decrease in Fe–O–Fe bond angle suggests the improvement in super-exchange interaction between Fe ions. From Table 4, it can be observed that the saturation and remnant magnetization for x = 0.025 is more than that for x = 0·000. The possible reason could be the decreases in average crystallite size of sample with the increase in substitution of Mn at Fe site of $Bi_{0.85}La_{0.15}Fe_{1-x}O_3$, and hence the uncompensated spins at the surface of sample increases, which contributes to net magnetization. Further increase in the concentration of Mn substitution results in decrement of the magnetization. Other researchers also observed the variation in magnetization due to substitution

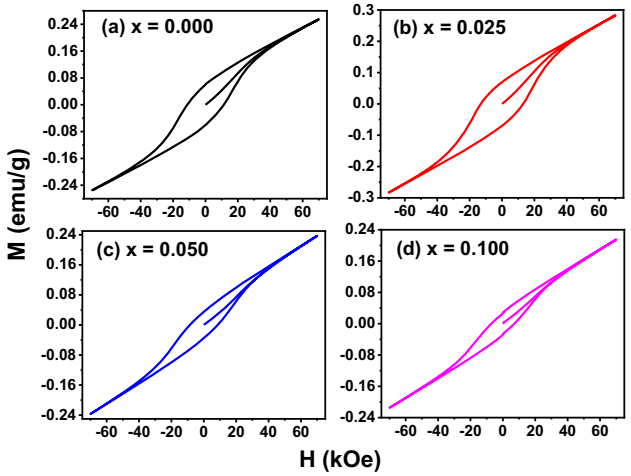

Fig.7 M−H loop of $Bi_{0.85}La_{0.15}Fe_{1-x}Mn_xO_3$ for x = 0.000–0.100

[15, 23]. It can be due to increase in collinear antiferromagnetic ordering contribution in the orthorhombic crystal symmetry (*Pbnm*, space group). In addition, Mn is non-magnetic in nature, the excess substitution of Mn breaks the Fe^{3+}–O–Fe^{2+} super exchange interaction and hence magnetization decreases for x > 0.025. Figure 7 shows that in $Bi_{0.85}La_{0.15}Fe_{1-x}Mn_xO_3$ polycrystalline sample, the hysteresis effect, that is with the increase in substitution concentration from x = 0.000 to x = 0.025, area of hysteresis loop increases and after that it decreases for x > 0.0250. This increase in hysteresis effect from x = 0.000 to x = 0.025 implies increase in deviation from linear behavior which exist due to cross linkage between weak ferromagnetic state (FM) and spatially modulated antiferromagnetic (AFM) state. This deviation is maximum for x = 0.025 and decreases significantly with the increase in substitution concentration for x > 0.025. Therefore, in order to depicts the usual AFM response the magnetic hysteresis loop of $Bi_{0.85}La_{0.15}Fe_{1-x}Mn_xO_3$ for x = 0.000 to x = 0.100 is drawn which is shown in Fig. 8. It implies that antiferromagnetic and/or paramagnetic both have contributed into the MH data.

The following equation was used to analyze the MH loop and determine the linear contribution from the PM and/or AFM components as well as to obtain the FM contribution in the MH Hysteresis loop [47–49].

$$M(H) = \left[2\frac{M_{FM}^{S}}{\pi}\tan^{-1}\left\{\left(\frac{H \pm H_{ci}}{H_{ci}}\right)\tan\left(\frac{\pi M_{FM}^{R}}{2M_{FM}^{S}}\right)\right\}\right] + \chi H \quad (4)$$

In Eq. 4, M_{FM}^{S} and M_{FM}^{R} are FM saturation and remnant magnetization respectively, H_{ci} is intrinsic coercivity, χ represents magnetic susceptibility, M is the observed magnetization, and H is the applied magnetic field. Here the first term represents FM part of hysteresis curve and the second term represents AFM and/or PM contribution for the $Bi_{0.85}La_{0.15}Fe_{1-x}Mn_xO_3$ for x = 0·000 to x = 0.100. Figure 8 represents the experimental data along with the fitted curve for PM and FM contributions for the $Bi_{0.85}La_{0.15}Fe_{1-x}Mn_xO_3$ samples. Table 4 summarizes the magnetic parameters that were extracted after analysis of Fig. 8. It indicates that contribution of FM part is maximum in case of x = 0.025 and it decreases significantly for high substitution concentration

Table 4 Magnetic parameters of $Bi_{0.85}La_{0.15}Fe_{1-x}Mn_xO_3$ for x = 0.000–0.100

Sample	M_r (emu/g)	M_r (emu/g) ferro-part	M_s at 70 kO_e (emu/g)	M_s at 70 kO_e (emu/g) ferro-part	H_c (kO_e)	H_c (kO_e) ferro-part
x = 0.000	0.060	0.061	0.254	0.077	11.168	16.718
x = 0.025	0.069	0.070	0.284	0.083	13.999	19.999
x = 0.050	0.037	0.037	0.237	0.048	8.999	17.999
x = 0.100	0.029	0.030	0.215	0.040	7.999	15.999

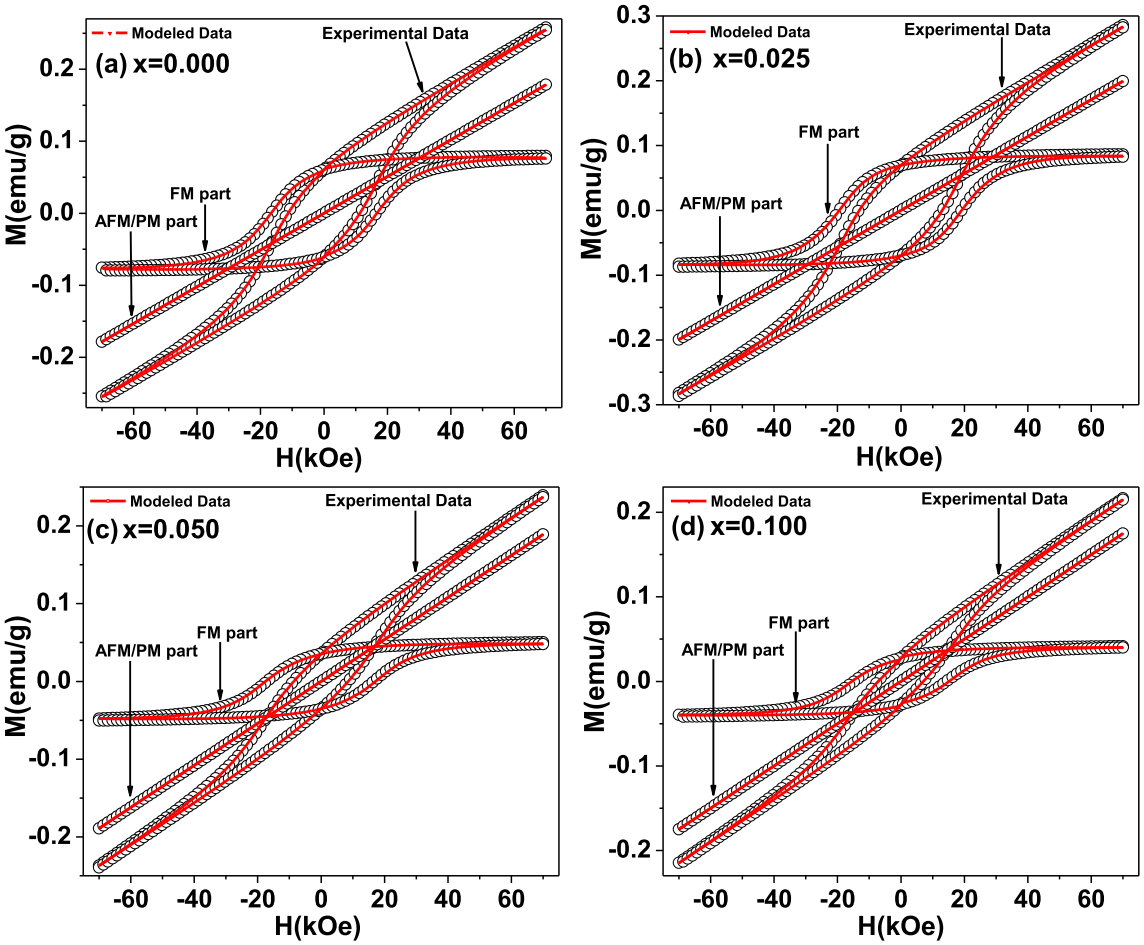

Fig. 8 Fitted M−H loop of $Bi_{0.85}La_{0.15}Fe_{1-x}Mn_xO_3$ for x = 0.000–0.100

(x > 0.025). The observed behavior of magnetization may be attributed to following reasons:

i. The uncompensated surface spin contribution, rises as average crystallite size falls,
ii. Cycloid spin structure suppression brought on by a reduction in average crystallite size and an increase in lattice strain,
iii. The resulting magnetization value is decreased by the collinear AFM ordering in the orthorhombic crystal symmetry (*Pbnm*, space group),
iv. The magnetic interaction with a neighboring Fe ion along the elongation (z axis) of the MnO_6 octahedron is AFM; however, engagement along the other principal axes results in FM interaction, which may boost the overall magnetization.

Table 4 shows that the remnant magnetization M_r increases upto x = 0.025 due to first two factors and for x > 0.025, M_r decreases due to last two factors. Similar trends are followed by M_s and H_c. Because of the variation in phase contribution and an increase in the number of grain boundaries by reduction in size of the grain, the rise in coercivity (H_c) occurs, which would prevent the mobility of the domain wall. But H_c decreases sharply for x > 0.025, inspite of having the same size as that of x = 0.025 ceramics. The reason could be the increase in orthorhombic phase contribution which ultimately results in the reduction in magnetic anisotropy. The crystallographic phase contribution represented in Table 2 shows a direct linkage between the magnetic properties and crystal symmetries in $Bi_{0.85}La_{0.15}Fe_{1-x}Mn_xO_3$ samples. Similar results for magnetization curves and magnetic parameters for substituted BFO are obtained by other researchers [39, 40].

3.4 UV–Vis study

Diffuse reflectance spectroscopy was utilized to study the variation of absorption spectra and energy band gap of $Bi_{0.85}La_{0.15}Fe_{1-x}Mn_xO_3$ samples. It reveals about the optical properties of the samples in UV–visible region. Figure 9 shows the UV–Vis absorbance spectra of $Bi_{0.85}La_{0.15}Fe_{1-x}Mn_xO_3$ samples for x = 0.000 to x = 0.100 in the range of 400–900 nm. The increase in optical absorption in the visible area, as seen in Fig. 9, aids in enhancing the material's photovoltaic characteristics. It also corresponds to the electronic transition from valence band to conduction band that is from O-2p state to Fe-3d state. This shows how the deformed cubic perovskite structure (lower symmetry), caused by internal chemical pressure, changes to orthorhombic symmetry (higher symmetry). This effect results from a size mismatch between the host and substituted cations which changes the local environment of FeO_6. Analysis of XRD and Raman spectroscopy also lend strong support for this observation. UV–Vis diffuse reflectance is then used in the formulation of Kubelka–Munk transformation which is used in the conversion of reflectance spectra to absorption spectra [50].

$$F(R) = \frac{(1 - R_\infty)^2}{2R_\infty} \quad (5)$$

where F(R) is the absorption coefficient and R_∞ is the reflectance at a particular wavelength.

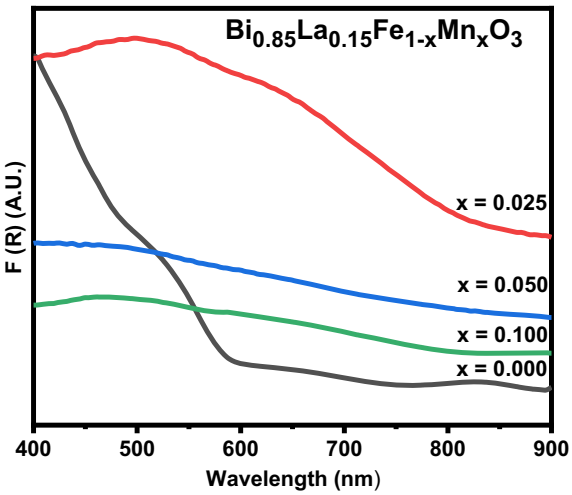

Fig. 9 UV–Visible absorption spectra of $Bi_{0.85}La_{0.15}Fe_{1-x}Mn_xO_3$ for x = 0.000–0.100

The band gap (E_g) of $Bi_{0.85}La_{0.15}Fe_{1-x}Mn_xO_3$ for x = 0·000 to x = 0.100 have been estimated using the Tauc's relation $(F(R)\ h\nu)\ \alpha\ (h\nu - E_g)^n$, where F(R) is the absorption coefficient, ν is the frequency of light, h is the Planck's constant and n = 2 for direct band gap [51]. The plots of $(F(R)\ h\nu)^2$ versus hν are presented in Fig. 10, and the corresponding energy band gap of the samples is obtained by extrapolating the linear component of the curves to the point of zero absorption [52]. The band gap value (E_g) for x = 0·000, 0.025, 0.050, and 0.100 are 2.17, 1.76, 1.69, and 1.60 eV respectively. Hence, it can be concluded that the band gap is decreasing with Mn substitution. Other researchers also observed the decrease in band gap due to substitution in BFO [10, 15].

The decrement in the value of band gap of $Bi_{0.85}La_{0.15}FeO_3$ by doping of Mn arises due to the presence of extra (impurity) band levels in between valence band and conduction band. Another factor that contributes to a lower band in a sample is the presence of irregular micro-strain in the particles brought on by a reduction in crystallite size, which modifies the energy levels and affects the edge of the absorption band [53]. In general, a variety of other variables, including as non-uniform lattice distortion, grain surface relaxation, dislocations, antiphase domain borders etc., contribute to micro-strain in nanocrystallites. However, according to Hauser et al. [54] the most common defect which significantly contribute to the micro-strain are oxygen vacancies, due to which extra sub bands are created which helps

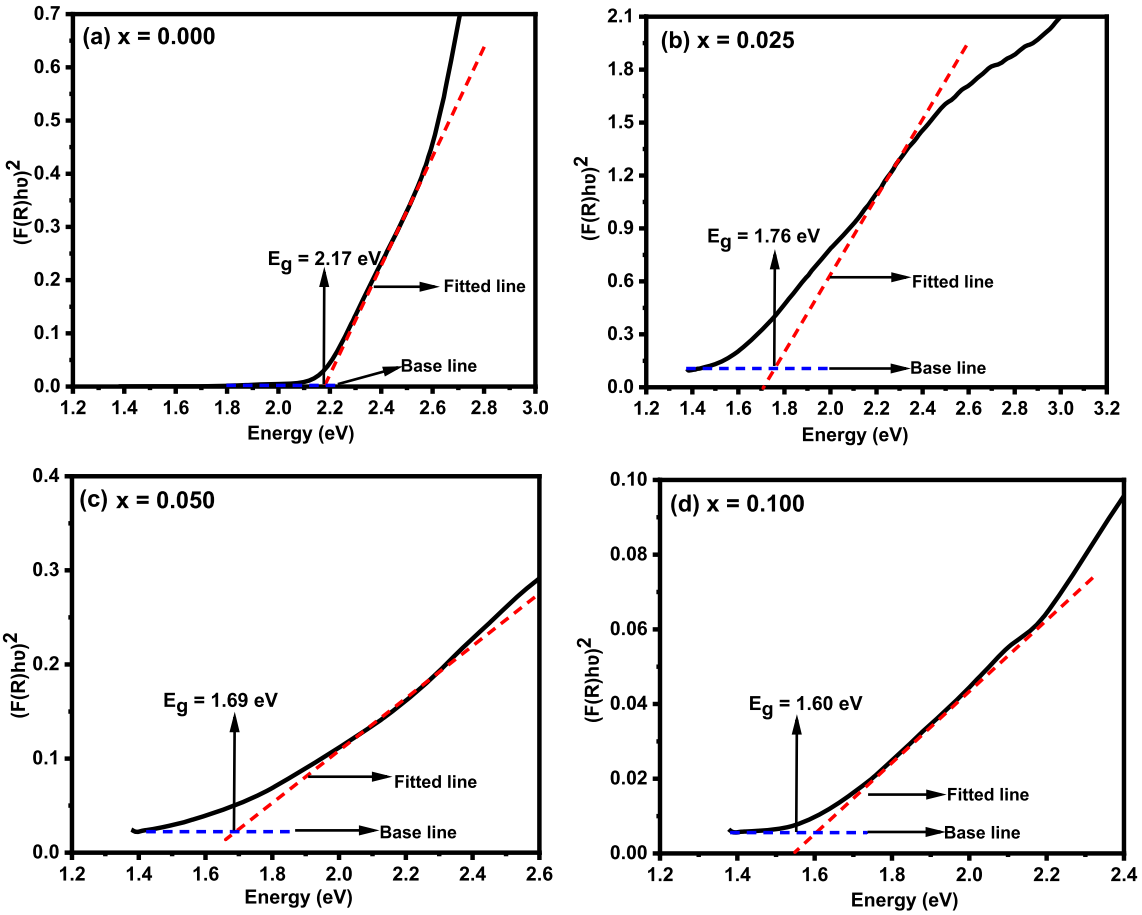

Fig. 10 Tauc Plot of $Bi_{0.85}La_{0.15}Fe_{1-x}Mn_xO_3$ for x = 0.000–0.100

in the reduction of energy band gaps and formation of more suitable photovoltaic materials.

4 Conclusions

The polycrystalline samples of $Bi_{0.85}La_{0.15}Fe_{1-x}Mn_xO_3$ samples were prepared by using tartaric acid modified sol–gel technique. The substitution of Mn at Fe site of $Bi_{0.85}La_{0.15}FeO_3$ results in a structural transition from rhombohedral symmetry (*R3c*, space group) to orthorhombic symmetry (*Pbnm*, space group). XRD patterns were refined using Rietveld Refinement and the result shows that the contribution from orthorhombic crystal symmetry (*Pbnm* space group) increases by increasing the concentration of Mn substitution. The same observation is also strongly supported by the analysis of Raman spectra for all the samples. The magnetization of $Bi_{0.85}La_{0.15}Fe_{1-x}Mn_xO_3$ reaches a maximum value of 0.284 emu/gm for x = 0.025, and decreases with the further increase in Mn substitution at Fe site. It might be because there is a higher proportion of the antiferromagnetic orthorhombic symmetry (*Pbnm* space) group than rhombohedral symmetry (*R3c*, space group). Due to collinear antiferromagnetic ordering, there exists the variation in M_s, M_r, and H_c parameters. UV–Vis spectroscopy also provides the evidence of this lattice deformation along with the decrease in the value of energy band gap with the increase in substitution concentration. All these findings conclude the formation of ceramics with better multiferroic properties.

Author contributions

All authors contributed to the study, conception and design. Material preparation, data collection, analysis and manuscript writing were performed by MS, SR, and RP. Supervision, investigation and review were

done by LK, MK and PK. All authors read and approved the final manuscript.

Funding

The authors declare that no funds, grants, or other support were received during the preparation of this manuscript.

Data availability

Data will be made available on the reasonable request.

Declarations

Competing interests The authors have no relevant financial or non-financial interest to disclose.

References

1. N.A. Hill, J. Phys. Chem. B **104**(29), 6694 (2000)
2. R. Seshadri, N.A. Hill, Chem. Mater **13**(9), 2892 (2001)
3. M. Fiebig, T. Lottermoser, D. Frohlich, A.V. Goltsev, R.V. Pisarev, Nature **419**, 818 (2002)
4. J. Zhang, Y.J. Wu, X.K. Chen, X.J. Chen, J. Phys. Chem. Solids **74**, 849 (2013)
5. J. Wang, J.B. Neaton, H. Zheng, V. Nagarajan, S.B. Ogale, B. Liu, D. Viehland, V. Vaithyanathan, D.G. Schlom, U.V. Waghmare, N.A. Spaldin, K.M. Rabe, M. Wuttig, R. Ramesh, Science **299**(5613), 1719 (2003)
6. Z.X. Cheng, A.H. Li, X.L. Wang, S.X. Dou, K. Ozawa, H. Kimura, S.J. Zhang, T.R. Shrout, J. Appl. Phys. **103**, 07E507 (2008)
7. J.F. Scott, J. Mater. Chem. **22**, 4567 (2012)
8. S. Rani, M. Shekhar, P. Kumar, S. Prasad, Appl. Phys. A **128**(12), 1046 (2022)
9. H. Xian, L. Tang, Z. Mao, J. Zhang, X. Chen, Solid State Commun. **287**, 54 (2019)
10. M.M. Rhaman, M.A. Matin, M.A. Hakim, M.F. Islam, Mater. Sci. Eng., B **263**, 114842 (2021)
11. S. Sharma, M. Kumar, G. Srinet, J.M. Siqueiros, O.R. Herrera, Ceram. Int. **47**(5), 6834 (2021)
12. Y. Liu, G. Tan, M. Guo, Z. Chai, L. Lv, M. Xue, A. Xia, X. Ren, J. Li, H. Ren, A. Xia, Ceram. Int. **45**(9), 11765 (2019)
13. G.S. Arya, R.K. Kotnala, N.S. Negi, J. Appl. Phys. **113**, 044107 (2013)
14. S. Chauhan, M. Kumar, S. Chhokar, S.C. Katyal, H. Singh, M. Jewariya, K.L. Yadav, Solid State Commun. **152**, 525 (2012)
15. P. Harshapriya, P. Kaur, D. Basandrai, Chin. J. Phys. **84**, 119 (2023)
16. D. Kothari, V.R. Reddy, A. Gupta, D.M. Phase, N. Lakshmi, S.K. Deshpande, A.W. Awashti, J. Phys.: Condens. Matter **19**, 136202 (2007)
17. Y.H. Lin, Q. Jiang, Y. Wang, C.W. Nan, L. Chen, J. Yu, Appl. Phys. Lett. **90**(17), 172507 (2007)
18. P.C. Sati, M. Arora, S. Chauhan, S. Chhoker, M. Kumar, J. Appl. Phys. **112**, 094102 (2012)
19. P.C. Sati, M. Arora, S. Chauhan, M. Kumar, S. Chhoker, Ceram. Int. **40**, 7805 (2014)
20. D. Do, J.W. Kim, J Am. Ceram. Soc. **94**(9), 2792 (2011)
21. P. Kumar, N. Shankhwar, A. Srinivasan, M. Kar, J. Appl. Phys. **117**(19), 194103 (2015)
22. A. Ianculescu, F.P. Gheorghiu, P. Postolache, O. Oprea, L. Mitoseriu, J. Alloys Compd. **504**, 420 (2010)
23. Y. Wang, J. Supercond. Novel Magn. **35**, 3565 (2022)
24. Z.X. Cheng, X.L. Wang, Y. Du, S.X. Dou, J. Phys. D: Appl. Phys. **43**, 242001 (2010)
25. S. Chauhan, M. Kumara, S. Chhokera, S.C. Katyal, H. Singh, M. Jewariya, K.L. Yadav, Solid State Comm. **152**, 525 (2012)
26. M. Połomska, B. Hilczer, I. Szafraniak Wiza, A. Pietraszko, B. Andrzejewski, Phase Transit. **90**, 24 (2017)
27. K. Sen, K. Singh, A. Gautam, M. Singh, Ceram. Int. **38**(1), 243 (2012)
28. S.R. Das, R.N.P. Choudhary, P. Bhattacharya, R.S. Katiyar, P. Dutta, A. Manivannan, M.S. Seehra, J. Appl. Phys. **101**, 034104 (2007)
29. M. Tariq, A. Shaari, K. Chaudhary, R. Ahmed, M.A. Jalil, F.D. Ismail, Physica B **414**, 650 (2023)
30. S. Chandel, P. Thakur, M. Tomar, V. Gupta, A. Thakur, Ceram. Int. **43**(16), 13750 (2017)
31. P. Kumar, M. Kar, J. Alloys. Compd. **584**, 566 (2014)
32. K. Aishwarya, R. Navamathavan, J. Alloy. Compd. **947**, 169452 (2023)
33. X.L. Liang, J.Q. Dai, J. Alloy. Compd. **886**, 161168 (2021)
34. A.K. Zak, W.A. Majid, M.E. Abrishami, R. Yousefi, Solid State Sci. **13**(1), 251 (2011)
35. Y. Shahmoradi, D. Souri, M. Khorshidi, Ceram. Int. **45**(5), 6459 (2019)
36. S. Fatima, S.I. Ali, M.Z. Iqbal, S. Rizwan, RSC Adv. **7**(57), 35928 (2017)
37. R. Pandey, L.K. Pradhan, P. Kumar, M. Kar, J. Phys. Chem. Solids **119**, 107 (2018)
38. J. Rodriguez Carvajal, Phys. B: Condens. Matter **192**(1–2), 55–69 (1993)

39. D.K. Pradhan, R.N.P. Choudhary, C. Rinaldi, R.S. Katiyar, J. Appl. Phys. **106**(2), 024102 (2009)
40. X. Zheng, Q. Xu, Z. Wen, X. Lang, D. Wu, T. Qiu, M.X. Xu, J. Alloy. Compd. **499**(1), 108 (2010)
41. M. Shariq, M. Imran, E.S. Gouda, A.R. Ansari, M.A. Siddiqui, M. Sowjanya, Arab. J. Sci. Eng. **45**, 475 (2020)
42. A.A. Porporati, K. Tsuji, M. Valant, A.K. Axelsson, G. Pezzottia, J. Raman Spectrosc. **41**, 84 (2010)
43. Y.J. Wu, X.K. Chen, J. Zhang, X.J. Chen, J. Appl. Phys. **111**(5), 053927 (2012)
44. J.M. Calderon-Moreno, S.S. Swamy, M. Yoshimura, Solid State Ion. **154–155**, 125 (2002)
45. Y.J. Wu, Z.X. Qin, X.K. Chen, J. Zhang, J. Liu, Z. Wu, X.J. Chen, J. Phys.: Condens. Matter **25**, 365401 (2013)
46. F.G. Garcia, C.S. Riccardi, A.Z. Simões, J. Alloy. Compd. **501**(1), 25 (2010)
47. F. Huang, Z. Wang, X. Lu, J. Zhang, K. Min, W. Lin, R. Ti, T.T. Xu, J. He, C. Yue, J. Zhu, Sci. Rep. **3**(1), 2907 (2013)
48. S. Duhalde, M.F. Vignolo, F. Golmar, C. Chiliotte, C.E.R. Torres, L.A. Errico, A.F. Cabrera, M. Renteria, F.H. Sanchez, M. Weissmann, Phys. Rev. B **72**, 161313 (2005)
49. L.R. Shah, H. Zhu, W.G. Wang, B. Ali, T. Zhu, X. Fan, Y.Q. Song, Q.Y. Wen, H.W. Zhang, S.I. Shah, J.Q. Xiao, J. Phys. D Appl. Phys. **43**, 035002 (2010)
50. A.F. AlHossainy, Bull. Mater. Sci. **39**(1), 209 (2016)
51. J. Tauc, R. Grigorovici, A. Vancu, Physica Status Solidi (b) **15**(2), 627 (1966)
52. H.M. Xian, Y.Q. Du, J. Zhang, X. Chen, Chin. J. Chem. Phys. **29**(5), 578 (2016)
53. P. Makuła, M. Pacia, W. Macyk, J. Phys. Chem. Lett. **9**(23), 6814 (2018)
54. A.J. Hauser, J. Zhang, L. Mier, R.A. Ricciardo, P.M. Woodward, T.L. Gustafson et al., Appl. Phys Lett **92**(22), 222901 (2008)